ORIGINAL ARTICLE

One-step solid-state synthesis of M_x-ZnBi$_2$O$_4$–Bi$_2$O$_3$ (M_x = Fe, Co, Ni, Eu, and Ho) nanocomposites and catalytic production of 3,4-dihydropyrimidin-2-(1H)-ones

Amene Mirzazadeh[1] · Alireza Hakimyfard[1] · Nemat Tahmasebi[1] · Leila Kafi-Ahmadi[2] · Shahin Khademinia[3]

Abstract

This paper presented the synthesis of M_x-ZnBi$_2$O$_4$–Bi$_2$O$_3$ (M_x = Fe, Co, Ni, Eu, and Ho) nanomaterials by a one-pot facile solid-state method at 650 °C for 10 h. Rietveld analysis data displayed the formation of ZnBi$_2$O$_4$–Bi$_2$O$_3$ composite in which ZnBi$_2$O$_4$ was crystallized as a main phase in orthorhombic crystal system with Pmmm space group. The investigation of optical properties indicated that doping the metal ions into the ZnBi$_2$O$_4$–Bi$_2$O$_3$ nanocomposite decreased the band-gap energy amount. Results indicated that the synthesized samples displayed paramagnetic behavior without any preferred magnetization direction. However, the data indicated that Co^{3+}-doped ZnBi$_2$O$_4$ showed highest magnetization value. In addition, cyclic voltammetry (CV) data and low EIS values revealed a pseudocapacitor behavior of the synthesized samples. Biginelli reaction to synthesize heterocyclic DHPMs compounds was applied to evaluate the catalytic performance of the samples. Results indicated that the synthesis yields of DHPMs at optimum condition were 92% and 96% for undoped and Eu-doped ZnBi$_2$O$_4$–Bi$_2$O$_3$, respectively.
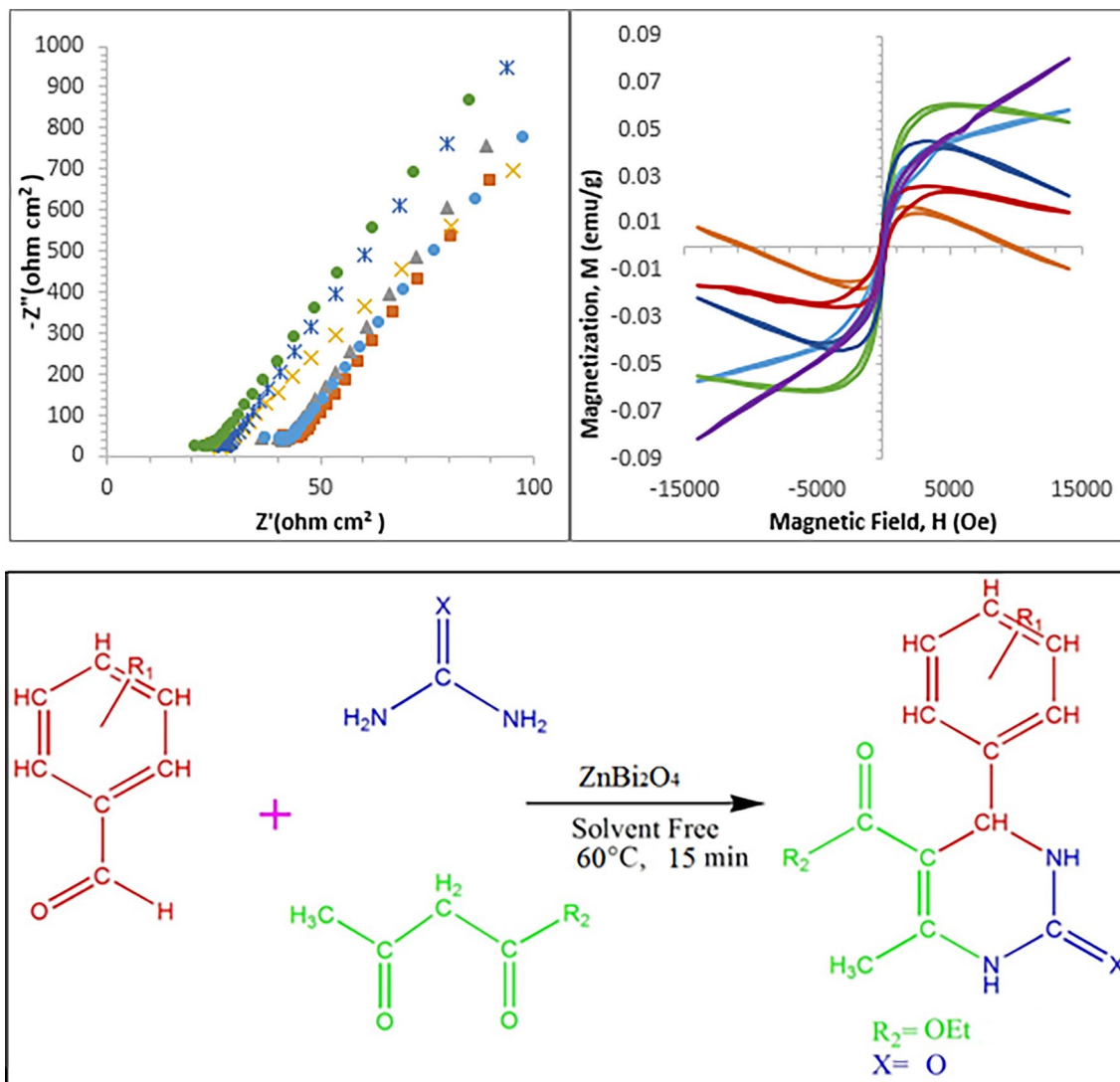
✉ Nemat Tahmasebi
  tahmasebi@jsu.ac.ir

1 Department of Physics, Faculty of Science, Jundi-Shapur University of Technology, Dezful, Iran

2 Department of Inorganic Chemistry, Faculty of Chemistry, Urmia University, Urmia, Iran

3 Department of Inorganic Chemistry, Faculty of Chemistry, Semnan University, Semnan, Iran

Graphical abstract

Keywords $ZnBi_2O_4$ · Solid state · Nanocomposite · Electrochemical property · Biginelli

1 Introduction

In recent years, $ZnBi_2O_4$ as a p-type semiconductor with a normal spinel structured material (A = a transition metal ion with d^{10} configuration and B = non transition metal that no CFSE is involved) widely has been used as photocatalyst to remove organic compounds [1–4]. Due to the magnetic relation between ZnO and Bi_2O_3, $ZnBi_2O_4$ compounds can be assumed as catalyst for various applications [5–7]. The p-type $ZnBi_2O_4$ is one of the suitable semiconductors for forming a p–n heterojunction with metal oxides [6]. It has been reported that $ZnBi_2O_4$ has a relatively small direct band-gap energy at 2.2–2.9 eV. However, it is a good value for visible-light-induced applications, but due to the high rate charge carrier recombination, the compound cannot be used as an efficient catalyst. Therefore, the catalytic performance of $ZnBi_2O_4$ is increased by compositing the compound with the other semiconductor materials and/or doping some elements into the host crystal system [8–15]. Due to the low band-gap energy of Bi^{3+}-based compounds, the materials can be used as visible light-induced catalyst/photocatalyst due to the absorbing light in visible region [14, 16–18]. $ZnBi_2O_4$ has been fabricated by several routs including oxidation–reduction and co-precipitation [5, 6], precipitation [19], solid state using ZnO and Bi_2O_3 at respective and step-by-step heat treatments from 200 to 800 ˚C

for 27 h [11], chemical co-precipitation [3, 20], reflux [21], and hydrothermal [7]. DHPMs compounds have been produced by the Biginelli reactions in one-step process using metal oxides as catalyst to facilitate the reaction conditions [22–25]. However, there is no report in the literature for the application of $ZnBi_2O_4$ nanocomposites as catalyst in the Biginelli reaction.

The current study introduces the fabrication of M_x-$ZnBi_2O_4$–Bi_2O_3 (M_x = Fe, Co, Ni, Eu and Ho) nanomaterials by a facile solid-state reaction in one-step rout at 650 °C for 10 h. Up to now, synthesis of the pure and the metal ion-doped $ZnBi_2O_4$ nanocomposites have not reported by the present conditions. The synthesized samples are investigated by several techniques including XRPD, FTIR, FESEM, UV–Vis, VSM, and CV. The catalytic performance of the synthesized nanocomposites is studied for the first time to synthesize DHPMs compounds by the Biginelli reactions.

2 Materials and methods

2.1 Preparation of catalyst

The initial compounds were of analytical grade and used without any purification. The following process was used to prepare $ZnBi_2O_4$–Bi_2O_3 nanocomposites by mixing and grounding 1.46 g (1.0 mol) of $Bi_5O(OH)_9(NO_3)_4$ and 0.15 g (0.5 mol) of $Zn(NO_3)_2.6H_2O$ in a mortar and then transferring into a 25 mL ceramic crucible. The obtained powder was treated thermally at 650 °C for 10 h (S_1). To synthesize the doped nanomaterials, 0.01 g (0.024 mol) of $Fe(NO_3)_3.9H_2O$ (S_2), 0.01 g (0.034 mol) of $Co(NO_3)_2.6H_2O$ (S_3), 0.01 g (0.034 mol) $Ni(NO_3)_2.6H_2O$ (S_4), 0.01 g (0.028 mol) Eu_2O_3 (S_5), and 0.01 g (0.026 mol) Ho_2O_3 (S_6) were used as dopant materials that were ground with the bismuth nitrate and zinc nitrate and heated at 650 °C for 10 h.

2.2 Apparatus

X-ray powder diffractometer D5000, *FullProf* software, a Philips XL30 scanning electron microscope (Philips, Amsterdam, The Netherlands) equipped with energy-dispersive X-ray (EDX) spectrometer, an Analytik Jena Specord 40 apparatus, a SHIMADZU FTIR instrument, and a vibrating sampling magnetometer were used to characterize and study the physical properties of the as-produced nanocomposites. Bulk elemental analysis was performed on an inductively coupled plasma atomic emission spectroscopy (ICP-OES), Specto Genesis, Germany. A thin-layer chromatography (TLC) on glass plates coated with silica gel 60 F254 was used to confirm the production of the DHPMs derivatives. The melting points of the DHPMs compounds were measured by a Thermo scientific 9100 device.
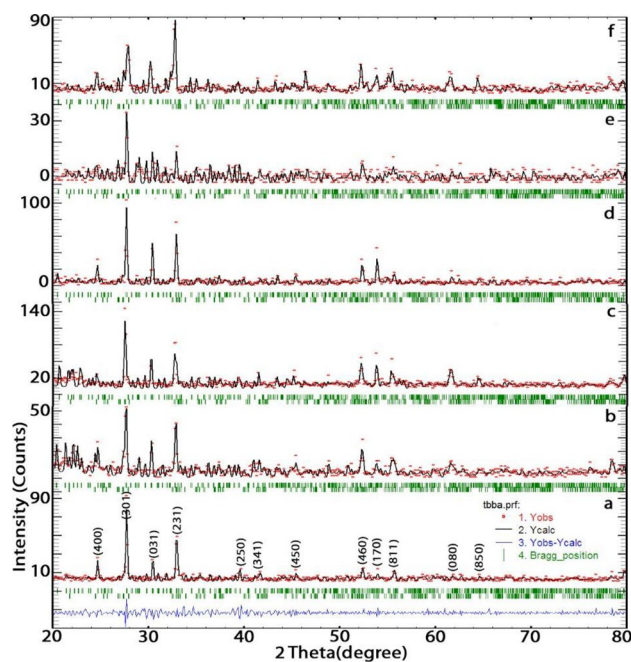
Fig. 1 XRPD patterns and the Rietveld analysis data of the synthesized samples, where **a** S_1, **b** S_2, **c** S_3, **d** S_4, **e** S_5, and **f** S_6

2.3 General procedure to synthesize DHPMs

DHPMs derivatives were fabricated by mixing benzaldehyde, ethyl acetoacetate, and urea at the molar ratio of 1:1:1.2, respectively, and certain amount of catalyst in a glass tube immersed in an oil bath. The mixture was stirred by a magnetic stirrer at a constant rate and certain designed time and temperature. When the reaction time was elapsed, the solid product was collected and washed by distilled water to separate the unreacted raw materials. Recrystallization of the washed DHPMs was done at room temperature to pure and measure the melting point of the prepared derivatives. Reaction yield of the final products was calculated by mmole fraction of the product to the raw material

$$R\% = \left(\frac{mmole\ of\ product}{mmole\ of\ raw\ material} \right) \times 100.$$

3 Results and discussion

3.1 Characterization of catalyst

Figure 1 a-f presents XRPD patterns and the Rietveld analysis data of $ZnBi_2O_4$–Bi_2O_3 nanocomposites. Red, black and blue lines are experimental, theoretical, and the difference between experimental and theoretical data, respectively. The characteristic peaks at 24.65, 27.64, 30.31,

Table 1 Lattice parameters, grain size, interplanar spacing, dislocation density, strain, specific surface area, and Rietveld refinement data of the as-prepared nanocomposites

Sample	2θ	$B_{1/2}$	a	b	c	V	d_{Bragg}	d	D	$\delta \times 10^{-3}$	$\varepsilon \times 10^{-3}$	ρx	SSA	χ^2	Counts
S_1	27.67	0.00324	14.43	11.99	4.34	751	3.22	3.22	44	0.517	0.785	0.4844	2.8	1.09	93
S_2	27.61	0.00368	14.41	12.06	4.36	757	3.23	3.23	39	0.657	0.893	0.4800	3.2	1.39	54
S_3	27.78	0.00323	14.41	12.08	4.31	751	3.21	3.21	44	0.517	0.785	0.4844	2.8	1.79	147
S_4	27.65	0.00324	14.44	12.01	4.34	753	3.22	3.22	44	0.517	0.786	0.4830	2.8	1.51	105
S_5	27.69	0.00323	14.47	12.01	4.32	751	3.22	3.22	44	0.517	0.785	0.4840	2.8	1.07	34
S_6	27.70	0.00323	14.45	12.12	4.32	758	3.22	3.22	44	0.517	0.785	0.4799	2.8	1.43	66

32.86, 35.22, 39.49, 41.62, 45.36, 52.30, 53.90, and 55.49 mentioned in the figure correspond to the orthorhombic $ZnBi_2O_4$ crystal system with Pmmm space group [14]. Besides, Bi_2O_3 was found as a secondary crystal phase in the mixture [5, 18]. As shown in Fig. 1, the intensity of the peaks changes by doping metal ions into $ZnBi_2O_4$ crystal system. Besides, it is found that doping Ho^{3+} changes the intensity proportion of the (301) plane to (231) plane showing the fact that the crystal growth direction of the crystal changes by doping Ho^{3+} into the crystal system. According to the metal ions radii of Zn^{2+} (IV) 0.6, (VI) 0.74, Bi^{3+} (VI) 1.03, Fe^{3+} (IV) 0.49, (VI) 0.55, Co^{3+} (VI) 0.55, Ni^{2+} (4sq) 0.49, (VI) 0.69, Eu^{3+} (VI) 0.95, and Ho^{3+} (VI) 0.90 Å, because the doping process does not change the unit cell volumes of the synthesized samples, it can be concluded that the dopant ions are intercalated in hexagonal BiO_6 crystal cavity.

Scherrer equation was applied to calculate the grain size of the as-prepared samples (Table 1)

$$D = \frac{K\lambda}{B_{\frac{1}{2}}\cos\theta}.$$

Dislocation density (δ) of the as-synthesized samples was calculated by the following relationship (Table 1):

$$\delta = \frac{1}{D^2}.$$

Interplanar spacing values were calculated by Bragg and the below equations (Table 1)

$$\frac{1}{d^2} = \left(\frac{h^2}{a^2} + \frac{k^2}{b^2} + \frac{l^2}{c^2}\right).$$

By choosing the peak at about 27.7° with the (hkl) value of (301), the equation changes to the below form

$$\frac{1}{d^2} = \left(\frac{9}{a^2} + \frac{1}{c^2}\right).$$

The strain (ε) parameter was calculated by the below formula (Table 1)

$$\varepsilon = \frac{\beta_{hkl}\cos\theta}{4}.$$

The X-ray density (ρ_x) value was calculated by the below formula (Table 1)

$$\rho_{x = \frac{ZM}{Na.b.c}}, \tag{5}$$

where M is the molecular weight of $ZnBi_2O_4$ ($M_W = 547.3$ gmol^{-1}), N is the Avogadro number, Z is the number of formula unit per unit cell (Z = 4), and a, b, c are lattice parameters. The constant amounts of ρ_x indicated that no sensitive change due to the intercalation of impurity with different density and atomic weight was found.

The specific surface area (SSA) per unit volume is calculated using the below formula by measuring XRD density (ρ_{xrd}) and mean particle size (D) amounts

$$SSA = \frac{6000}{D\rho_{xrd}}. \tag{6}$$

FESEM images of the as-fabricated samples are shown in Fig. 2 a-f, respectively, for S_1-S_6. This figure shows that the morphology of the samples is a mixture of particle with bulk structure. Figure 2 a shows that the particle size of S_1 is about 80–150 nm. However, it shows that doping process (S_2) changes the morphology of the sample and slab structure is found. The thickness size of the slabs is about 40 nm. By changing the dopant ion type into the crystal system (S_4), the morphology changes to porous structure. No considerable change (S_5 and S_6) in the morphology is found when the dopant ion type is changed. It is clear that the particle sizes of S_5 and S_6 are about 40–50 nm.

The EDS analysis was used to determine the concentration of the metal ions on the surface of the synthesized nanocomposites. This analysis indicated the existence of Fe, Co, Ni, Eu, and Ho dopants in S_2, S_3, S_4, S_5 and S_6, respectively. In addition, the A% of dopant for these samples are 0.34, 0.68, 0.82, 0.53, and 0.67, respectively, for S_2 to S_6. To study the amount of the dopant types in the bulk of the synthesized samples, ICP-OES was used. According to the data, it was found that the amounts are 0.018, 0.023, 0.019, 0.015, and
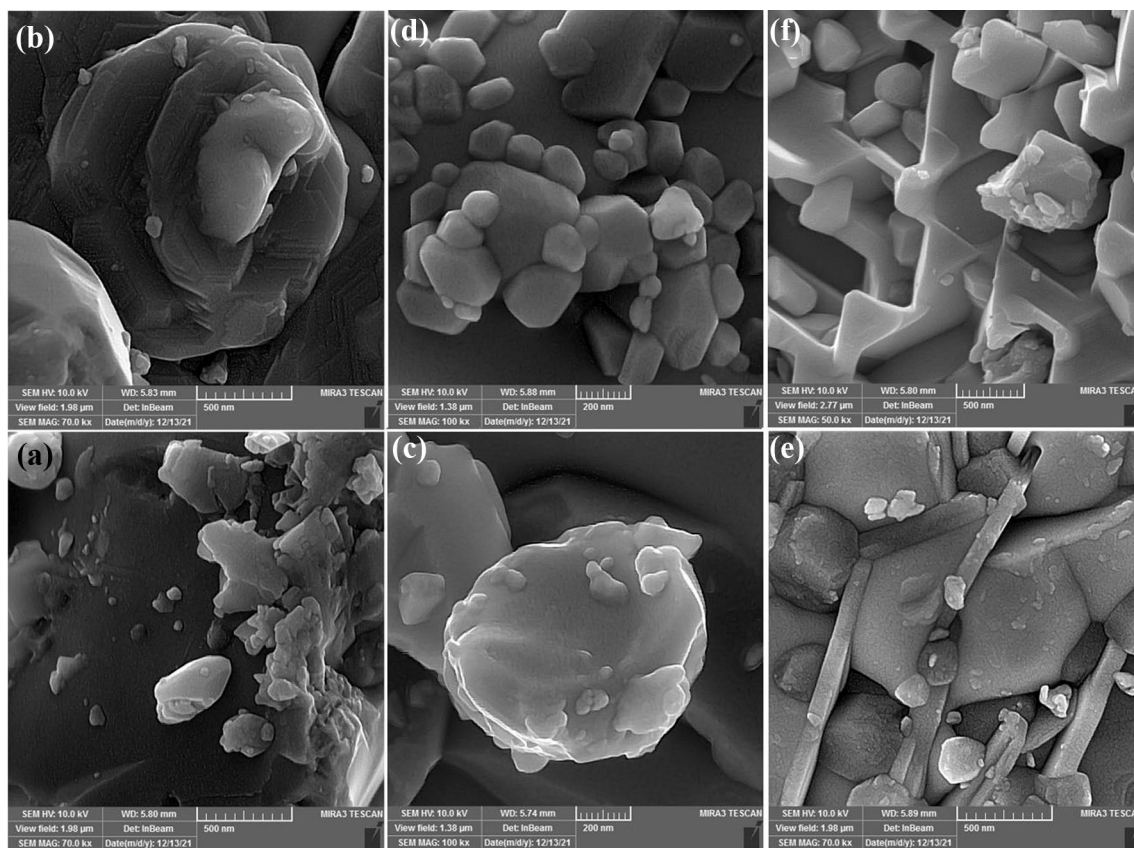
Fig. 2 FESEM images of **a** S_1, **b** S_2, **c** S_3, **d** S_4, **e** S_5, and **f** S_6

0.021, respectively, for S_2 to S_6, respectively. As could be found from the data, it is clear that the occupation of the dopant metal ions on the surface of the nanocomposites is more than their concentrations into the bulk of the samples (Fig. 3).

FTIR spectra of the as-synthesized samples are given in Fig. 4. The main absorption peaks of samples are located at 440, 550, 630, 780, 1628, 2376, and 3410 cm^{-1}. The absorption band at about 545 cm^{-1} is attributed to Zn–O-stretching mode. The peaks at 480–630 cm^{-1} are characteristic to Bi–O and Zn–O in ZnBi$_2$O$_4$ [26]. The peaks at about 400–900 cm^{-1} correspond to the band of metal–oxygen (M–O) [27–29]. The presence of these M–O bands means that the tetragonal structure is formed by zinc and bismuth oxides. The presence of peaks between 570 and 628 cm^{-1} confirmed the formation of the spinel belonging to the Bi–O-bond vibration [30, 31]. The absorption band at 430 cm^{-1} and 524 cm^{-1} is assigned to the tetrahedral ZnO$_4$ [15, 32, 33]. The bands at 3410 cm^{-1} and 1628 cm^{-1} are attributed to the existence of the adsorbed water (H–O–H) [16].

The magnetic behavior of the powder samples was investigated by VSM analysis. As shown in Fig. 5 a and b, the paramagnetic behavior of the fabricated samples was confirmed by the plots of M versus H at room temperature.

According to Fig. 5 a, the values of saturation magnetization (M_s) for S_1, S_2, S_3, S_4, S_5, and S_6 samples are 0.020, 0.040, 0.060, 0.045, 0.027, and 0.018 emu/g, respectively. The data indicated that the M_s value increases by doping Co^{3+} into the host crystal system. Moreover, the value of remanence magnetization (M_r) [defined as the residual magnetization, while the external magnetic field is zero (H = 0)] for S_1, S_2, S_3, S_4, S_5, and S_6 are 0.005, 0.008, 0.005, 0.01, 0.008 and 0.005 emu/g, respectively [34]. Because of the very small values of the Mr, we can conclude that the synthesized compounds have paramagnetic behavior. The squareness ratio magnitude ($M_{rs} = M_r/M_s$) is 0.25, 0.20, 0.08, 0.22, 0.30, and 0.28, respectively. Thus, it can be concluded that no preferred direction in magnetization is found for undoped and doped samples. Furthermore, coercive field (H_c) which is defined as the magnitude of reverse magnetic field to remove the magnetization effect is considered as one of the main characteristics of paramagnetic materials. As could be found from the magnified loop (Fig. 5 b), it is seen that S_5 has the largest H_c value of about 200 Oe indicating the more reverse magnetic force to remove the magnetization effect of the sample.

Figure 6 a and b shows the UV–Vis spectra and direct band-gap energy values plots of the synthesized samples,
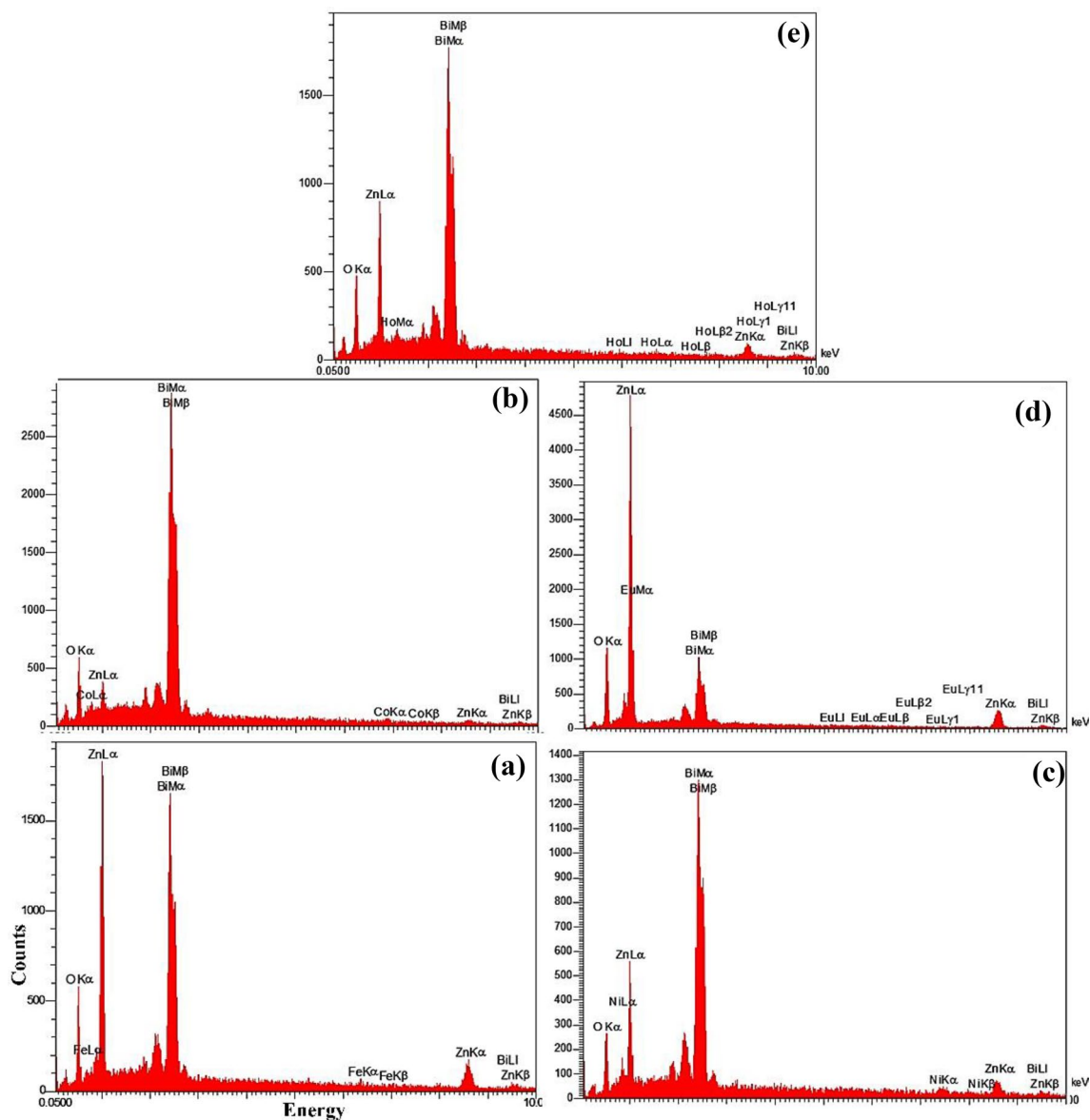
Fig. 3 EDX spectra of **a** S_2, **b** S_3, **c** S_4, **d** S_5, and **e** S_6

respectively. According to Fig. 6 a, it can be concluded that the nanomaterials possess typical strong absorption in the range of 430–600 nm for S_3. The $(\alpha h\nu)^2 = A(h\nu - E_g)$ equation is used to calculate the direct band-gap energy value [35]. As shown in Fig. 6 b, all the samples display a strong band structure at the energy range of 1.7 – 2.7 eV. The smallest and largest direct band-gap energies are found for S_3 ($E_g = 1.7$ eV) and S_1 ($E_g = 2.7$ eV), respectively. It can be concluded that the doping of metal ions decreases the Eg compared to the undoped $ZnBi_2O_4$ nanomaterial.

3.2 Electrochemical property

The electrochemical properties of the synthesized samples were examined by cyclic voltammetry (CV) in a three-electrode cell containing working, reference, and counter electrodes. In this work, graphite powder, silicon oil, and $ZnBi_2O_4$ powder were mixed in the ratio of 10:80:10 to prepare the working electrode. Figure 7 a and b show the electrochemical impedance spectroscopy (EIS) plot of the samples. It is found that Z values for the synthesized samples are about 20 to 40 Ω/cm^2, and the smallest value belongs to S_5. Furthermore, it should be mentioned that higher EIS
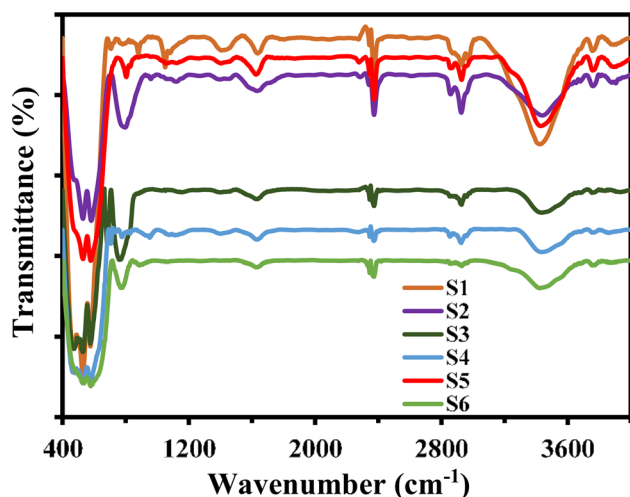
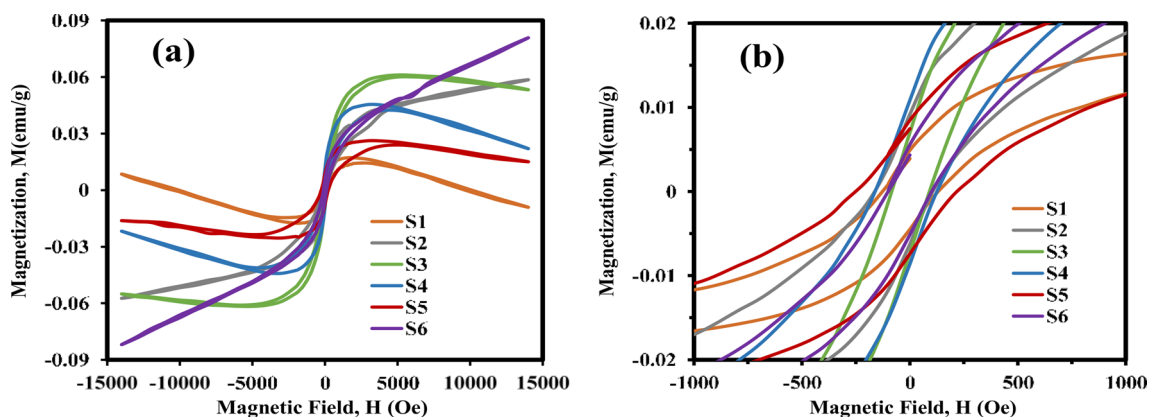**Fig. 4** FTIR spectra of the synthesized samples

values shows the weaker charge transfer [36]. As shown in Fig. 7 b, the area of Nyquist arc for S_5 is less than the other samples which is attributed to the higher charge transfer rate of this sample. Further, the slope of the curve is near to 90° representing the behavior of good capacitor behavior which is consistent with the CV results [36].

Figure 7c-h exhibits the cyclic voltammograms of the samples in 1 $molL^{-1}$ NaOH aqueous solution between 0 and +1.5 V at different scan rates. The CV curves of the nanocomposites do not show a typical rectangular shape, confirming no pure electric double-layer capacitive behavior and no oxidation–reduction of the nanomaterials at the cell potential range. The EW is an important characteristic that should be identified for solvents and electrolytes used in electrochemical applications. According to the graphs, it is found that the current density values are in the ranges of 0 to +0.7, 0 to 0.6, 0 to 0.70, 0 to 0.6, 0 to 0.7, and 0 to 0.6 V, respectively, for S_1, S_2, S_3, S_4, S_5, and S_6. Besides, a small broad feature around
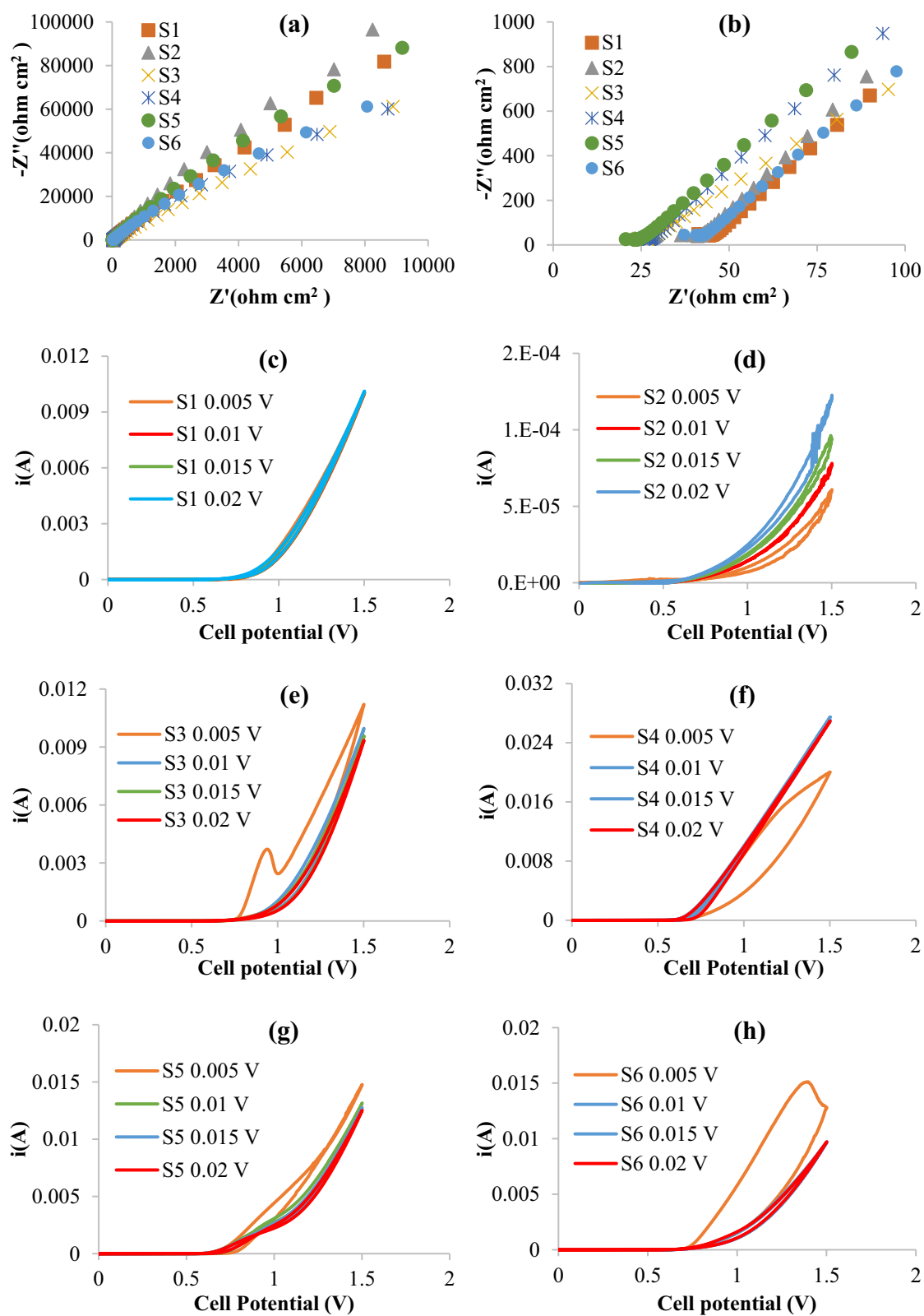

Fig. 5 M − H curves of the synthesized samples at room temperature
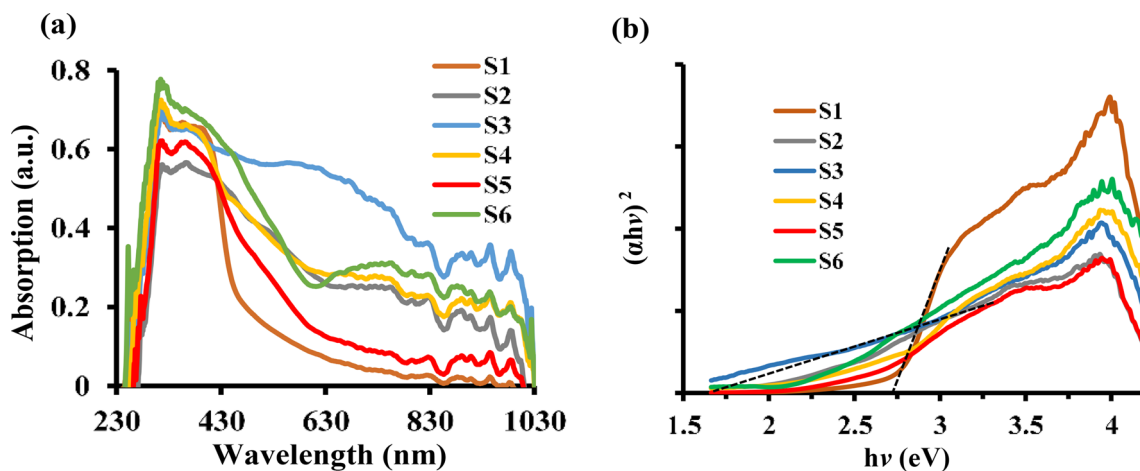
Fig. 6 **a** UV–Vis spectra and **b** band-gap determination plots of the synthesized nanocomposites

Fig. 7 **a**, **b** Nyquist and **c-h** CV plots of the synthesized nanocomposites

Table 2 Fabrication of the DHPMs compound using S_1–S_5 nanocatalyst at the optimized conditions

Entry	Ar	S_1 (%)	S_2 (%)	S_3 (%)	S_4 (%)	S_5 (%)	S_5 (%)	m.p(°C) S_1 [22, 39–43]	
1	C_6H_5CHO	92	90	88	93	96	95	202–204	202–203
2	$4\text{-}BrC_6H_4CHO$	89	86	87	89	91	92	212–214	213–215
3	$2\text{-}ClC_6H_4CHO$	78	75	75	80	82	81	215–217	216–219
4	$4\text{-}ClC_6H_4CHO$	90	84	86	92	93	92	212–214	213–215
5	$4\text{-}MeC_6H_4CHO$	89	82	84	91	93	95	215–217	214–216
6	$4\text{-}MeOC_6H_4CHO$	77	72	72	71	82	81	200–202	201–202
7	$4\text{-}O_2NC_6H_4CHO$	63	60	58	66	67	67	206–208	207–208
8	$2\text{-}HOC_6H_4CHO$	79	76	70	83	82	82	213–215	214–215
9	$4\text{-}HOC_6H_4CHO$	88	81	82	91	93	92	230–232	232–234

0 V indicated a small pseudocapacitive behavior. The data indicate that the samples shows a good onset potential and larger current density in CV curve implying a larger capacitance when the dopant ions are introduced into the host crystal system [37].

The following equation gives the charge discharge specific capacitance [38]

$$C = \frac{i \times \mathrm{d}t}{m(Vf - Vi)}.$$

In the equation, i is the applied current, dt is the discharging time, m is the mass of the active material coated on to the electrode, and (V_f-V_i) is the working potential window. In the present work, m is 0.01 g and i is 0.05 A/cm^2. The data are included in Table 2. The dt (s) values are 334, 164, 87, and 84 (S_1-S_5), and 662, 107, 83, and 82 (S_6), for 0.005, 0.01, 0.015 and 0.02 V/s scan rates, respectively. The C values are 2385, 1171, 621, and 600 (V_f-V_i=0.7), 2783, 1366, 725, and 700 (V_f-V_i=0.6). The C values for S_6 are 5516, 817, 691, and 683.

3.3 Catalytic activity of M_x-$ZnBi_2O_4$–Bi_2O_3 (M_x = Fe, Co, Ni, Eu, and Ho) nanocomposite

The present study determines the values of nanocatalyst, reaction time, and temperature on the reaction yield (yield (%)) using design expert software to optimize the mentioned parameters values. The possible combinations of the three factors with the response values are included in table S_1 (presented in the supplementary file). Three replicates at the center of the factors are considered to validate the applied model by ANOVA (Table S_2). The low and high levels of the above mentioned factors were coded as -1 and +1, respectively (Table S_3). Linear response model was confirmed by analyzing the ANOVA data. The relation between the three factors (catalyst, time, and temperature) and the yield of the Biginelli reaction, Y%, is shown below.

$$R_1 = +51.65 + 15.52A + 9.95B + 15.36C. \tag{1}$$

It is clear that the effect of catalyst is higher than the other factors. However, the effects of time and catalyst on the reaction yield are close to each other. The data shown in table S_2 indicate that the p value of the regression is smaller than 0.05. Therefore, the proposed model is significant at a high confidence level (95%). The p value of lack of fit is greater than 0.05 confirming the significance of the model. R-square and adjusted-R-square parameters are used to express the quality of fit of the linear model equation. R^2 is 0.98 confirming a high degree of correlation between the response and the independent factors. Besides, the high values of adjusted regression coefficient (R^2-adj = 0.97) and predicted regression coefficient (R^2-prd = 0.96) confirm more the desirability of the proposed model.

The optimization results obtained by the full factorial design showed that the optimum condition for the synthesis of the DHPMs was 0.03 g of catalyst, 60 ºC reaction temperature, and 15 min reaction time (Table S_2). The optimized condition was used for the synthesis of other derivatives. Schematic image is presented below to show a summary of the Biginelli reaction pathway (Scheme 1).

Figure 8 a-d represents the 3D and cube plots relate to the interactions of AB, AC, and BC. The data presented in the figure reveal that the DHPMs production percentage enhances when the catalyst amount and reaction time increase at a certain reaction temperature. This is because of the availability of high surface area of catalyst for the raw materials molecules to produce the targets. As could be found from Fig. 8 d, the cube plot shows the impact of all of the parameters together on the reaction yield. The experimental residual data are included in the supplementary file (figure S2).

Table 2 shows the catalytic activity of S_1 and S_5 under optimized conditions using different starting material derivatives in relation to the obtained melting points of the synthesized DHPMs compounds. As can be seen from the data, it is clear that the catalytic performance of S_5 is higher than that of S_1 for almost all derivatives.

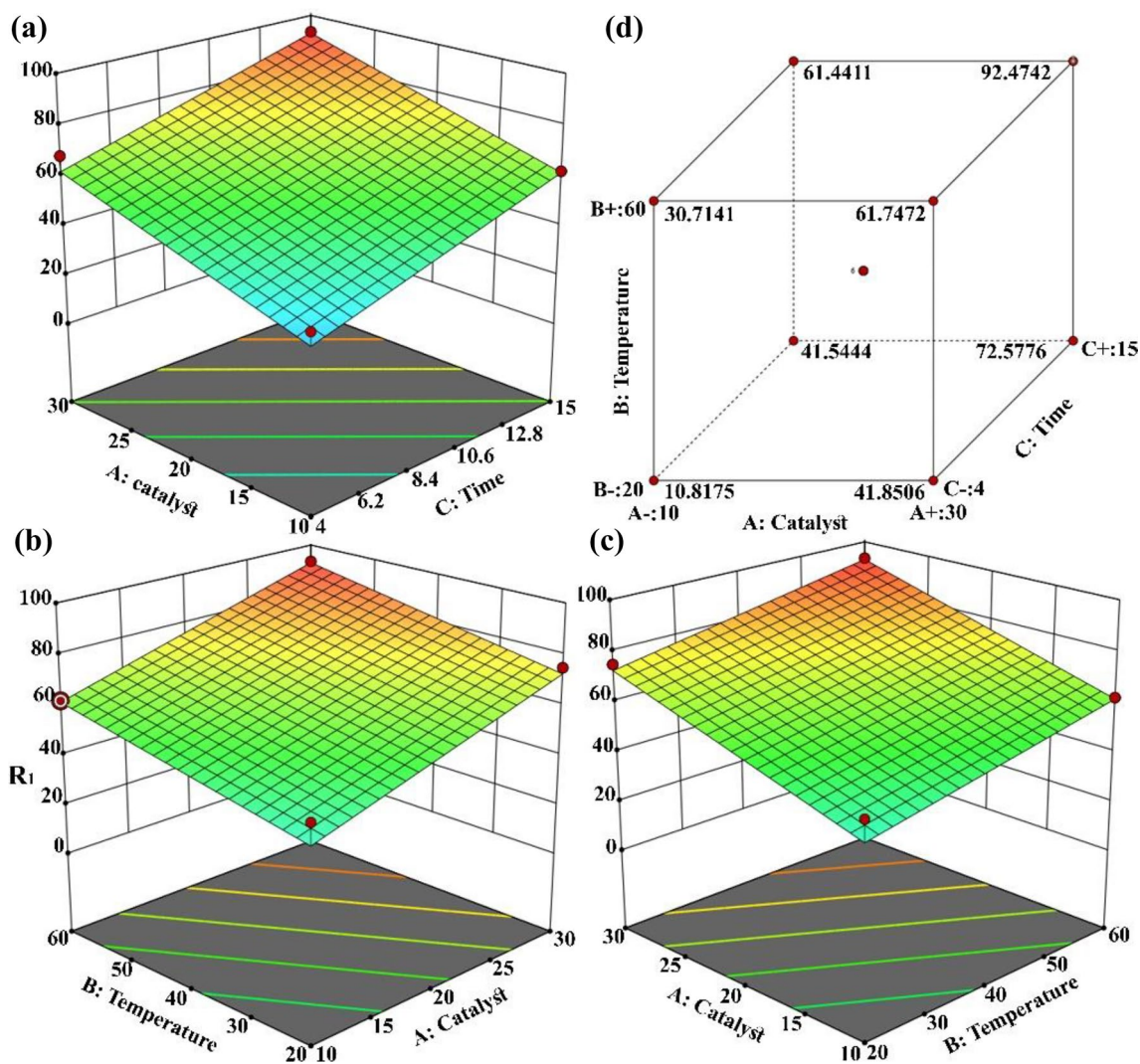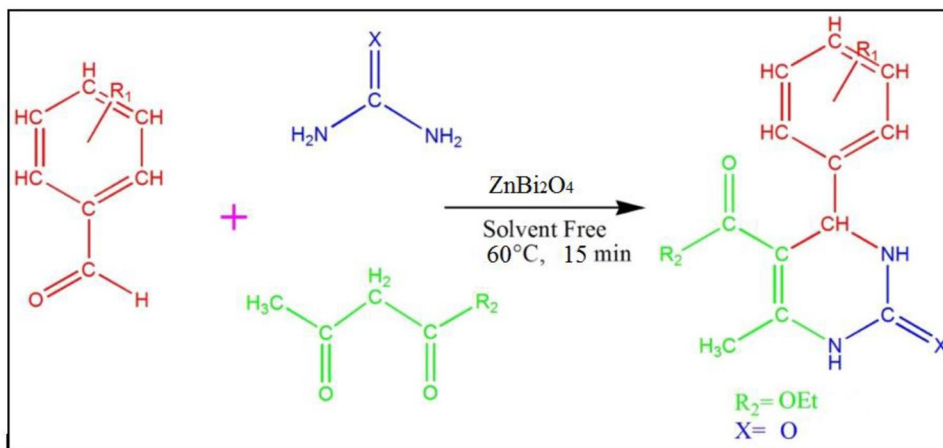**Scheme 1.** Schematic representation of the reaction pathway for the synthesis of DHPMs

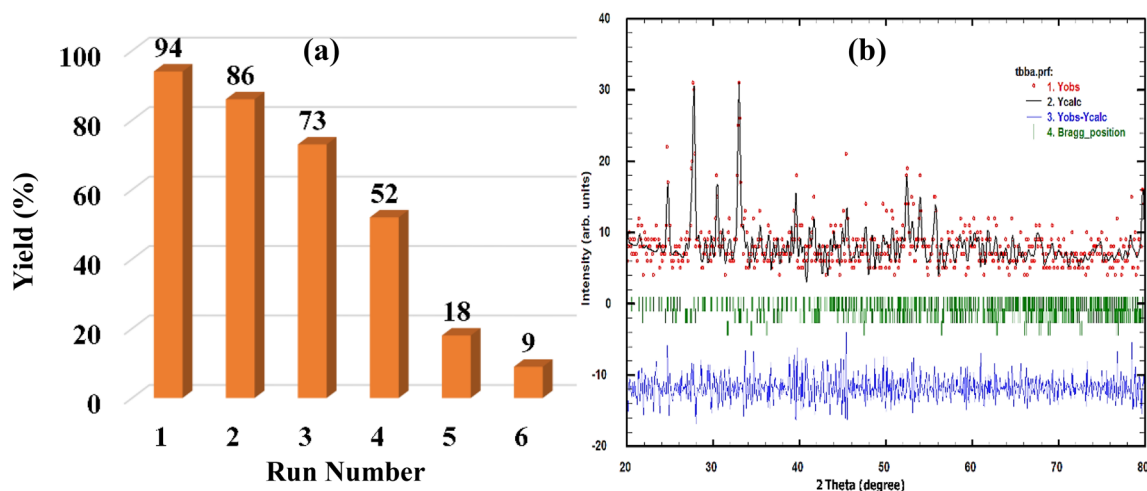**Fig. 8** **a-c** 3D and **d** cube plots of interactions of the factors for the Biginelli reaction

Fig. 9 a Reusability and **b** XRPD patterns of S_1 after 4 runs of the catalytic reaction

Table 3 Comparison study for the catalytic Biginelli reactions

Entry	Nanocatalyst	Yield (%)	Ref.
1	$ZnBi_2O_4$	96	Present work
2	$Bi_2V_2O_7$	89	[38]
3	$Bi_2Mn_2O_7$	96	[39]
4	Doped-$Sr_2Nb_2O_7$	92	[40]
5	$Sr_2As_2O_7$	96	[41]
6	NiO	97	[42]
7	Doped-$Bi_2Mn_2O_7$	82	[43]

Reusability of S_1 nanocatalyst in the present Biginelli reactions was tested. As could be found from Fig. 9 a, it is clear that the catalyst efficiency is acceptable until run 4. Besides, Fig. 9 b shows XRD pattern of S_1 after four runs of the catalytic reaction. It shows that there is a decomposition of $ZnBi_2O_4$ to ZnO [44] and Bi_2O_3 [18, 45]. Also, the intensity of the peaks that is attributed to the crystal nature of the sample is decreased.

To show the efficiency of the present synthesized nanocatalyst, the catalytic yields of the previous reported works were compared to the present study (Table 3). The data confirmed the high ability of the synthesized samples to catalyze the Biginelli reaction.

4 Conclusion

The current experimental study introduced the synthesis of M_x-$ZnBi_2O_4$–Bi_2O_3 (M_x = None, Fe, Co, Ni, Eu, and Ho) nanocomposites by a facile solid-state method. The as-synthesized samples were characterized and investigated by different physical and electrochemical analysis such as

XRD, Rietveld, FESEM, EDX, FTIR, UV–Vis, VSM, and CV. Results indicated that the Co-doped $ZnBi_2O_4$–Bi_2O_3 sample displayed smallest direct band-gap energy value with the band-gap energy of 1.7 eV. Besides, the VSM data confirmed that the highest magnetic property was found for Ni-doped $ZnBi_2O_4$–Bi_2O_3 nanocomposite. CV data revealed that the synthesized samples had capacitor behavior. The catalytic activity of the nanocomposites was evaluated by measuring their performance to prepare DHPMs derivatives. Results indicated that the synthesized samples were highly efficient and the synthesized yields at the optimum conditions (catalyst amount = 31 mg, temperature = 60 °C, and reaction time = 15 min) for undoped and Eu-doped sample were 92% and 96%, respectively. According to the present work, a new class of materials with unique physical, electrochemical, and catalytic properties were introduced. The nanocomposites can be used in future works as photocatalyst under visible light for degradation of various pollutant dyes and catalyst for the synthesis of organic compounds in chromene, imidazole, tetrazole, etc. reactions.

Declarations

References

1. E. Dvininov, M. Ignat, P. Barvinschi, M.A. Smithers, E. Popovici, J. Hazard. Mater. **177**, 150 (2010)
2. G.R. Williams, D. O'Hare, J. Mater. Chem. **16**, 3065 (2006)
3. J. Zhang, Y. Jiang, W. Gao, H. Hao, J. Mater. Sci.: Mater. Electron. **26**, 1866 (2015)
4. K. Goswami, R. Ananthakrishnan, New J. Chem. **41**, 4406 (2017)
5. N.T.M. Tho, D.N.N. Khanh, N.Q. Thang, Y.I. Lee, N.T.K. Phuong, Sci. Pollut. Res. **27**, 11127 (2020)
6. N.T.M. Tho, B.T. Huy, D.N.N. Khanh, N.Q. Thang, N.T.P. Dieu, B.D. Duong, N.T.K. Phuong, Chem. Select. **3**, 9986 (2018)
7. N.T.M. Tho, B.T. Huy, D.N.N. Khanh, H.N.N. Ha, V.Q. Huy, N.T.T. Vy, D.M. Huy, D.P. Dat, N.T.K. Phuong, Korean J. Chem. Eng. **35**, 2442 (2018)
8. M. Pirhashemi, A. Habibi-Yangjeh, S.R. Pouran, J. Ind. Eng. Chem. **62**, 1 (2018)
9. M. Shekofteh-Gohari, A. Habibi-Yangjeh, M. Abitorabi, A. Rouhi, Crit. Rev. Environ. Sci. Technol. **48**, 806 (2018)
10. X. He, C. Zhang, J. Mater. Sci. **54**, 8831 (2019)
11. A. Akhundi, A. Habibi-Yangjeh, M. Abitorabi, S. Rahim Pouran, Catal Rev. **61**, 595 (2019)
12. R. Koutavarapu, G. Lee, B. Babu, K. Yoo, J. Shim, J. Mater. Sci. Mater. Electron. **30**, 10900 (2019)
13. S.G. Kumar, K.K. Rao, Appl. Surf. Sci. **391**, 124 (2017)
14. J. Zhang, Y. Jiang, W. Gao, H. Hao, J. Mater. Sci. Mater. Electron. **26**, 1866 (2015)
15. M. Eddya, B. Tbib, K. El-Hami, J. Mater. Sci. Mater. Electron. **9**, 3087 (2018)
16. R. Nithya, S. Ayyappan, J. Photochem. Photobiol. A Chem. **398**, 112591 (2020)
17. R.S. Yadav, J. Havlica, I. Kuřitka, Z. Kozakova, M. Palou, E. Bartoníčková, M. Boháč, F. Frajkorová, J. Masilko, M. Hajdúchová, V. Enev, J. Supercond. Nov. Magn. **28**, 1417 (2015)
18. C. Sakthivel, A. Nivetha, G. Thiruppathi, P. Sundararaj, I. Prabha, New J. Chem. **47**, 571 (2023)
19. V.H. Nguyen, M. Mousavi, J.B. Ghasemi, Q.V. Le, S.A. Delbari, A.S. Namini, M. Shahedi Asl, M. Shokouhimehr, M. Mohammadi, J. Phys. Chem. C. **124**, 27519 (2020)
20. O. Baaloudj, A.A. Assadi, M. Azizi, H. Kenfoud, M. Trari, A. Amrane, A.A. Assadi, N. Nasrallah, Appl. Sci. **11**, 3975 (2021)
21. A. Habibi-Yangjeh, M. Pirhashemi, S. Ghosh, J. Alloys Compd. **826**, 154229 (2020)
22. S. Khademinia, M. Behzad, J. Nanostruct. **9**, 172 (2019)
23. M. Khashaei, L. Kafi-Ahmadi, S. Khademinia, A. Poursattar Marjani, E. Nozad, Sci. Rep. **12**, 8585 (2022)
24. E. Kolvari, N. Koukabi, M.M. Hosseini, Mol. Catal. **397**, 68 (2015)
25. L.M. Sanchez, Á.G. Sathicq, G.P. Romanelli, L.M. González, A.L. Villa, Mol. Catal. **435**, 1 (2017)
26. M. Pirhashemi, A. Habibi-Yangjeh, J. Colloid Interface Sci. **474**, 103 (2016)
27. Q. Geng, X. Zhao, X. Gao, S. Yang, G. Liu, J. Sol-Gel. Sci. Technol. **61**, 281 (2012)
28. H. Ramezanalizadeh, R. Peymanfar, N. Khodamoradipoor, Optik (Stuttg) **180**, 113 (2019)
29. S. Mobini, F. Meshkani, M. Rezaei, J. Environ. Chem. Eng. **5**, 4906 (2017)
30. G. Viruthagiri, P. Kannan, J. Mater. Res. Technol. **8**, 127 (2019)
31. J. Yang, T. Xie, C. Liu, L. Xu, Materials. **11**, 1359 (2018)
32. B. Pant, H.R. Pant, N.A.M. Barakat, M. Park, K. Jeon, Y. Choi, H.Y. Kim, Ceram. Int. **39**, 7029 (2013)
33. B. Pant, G.P. Ojha, H.Y. Kim, M. Park, S.J. Park, Environ. Pollut. **245**, 163 (2019)
34. A. Hakimyfard, N. Zalpour, F. Zarinabadi, J. Aust. Ceram. Soc. **58**, 817 (2022)
35. N. Tahmasebi, Z. Zadehdabagh, J. Aust. Ceram. Soc. **56**, 49 (2020)
36. B. Xu, S. Yue, Z. Sui, X. Zhang, S. Hou, G. Cao, Y. Yang, Energy Environ. Sci. **4**, 2826 (2011)
37. P. Connor, J. Schuch, B. Kaiser, W. Jaegermann, Z. Phys, Chem. **234**, 979 (2020)
38. C.R. Ravikumar, M.R. Anil Kumar, H.P. Nagaswarupa, S.C. Prashantha, A.S. Bhatt, M.S. Santosh, D. Kuznetsov, J. Alloys Compd. **736**, 332 (2018)
39. S. Khademinia, M. Behzad, H.S. Jahromi, RSC Adv. **5**, 24313 (2015)
40. S. Khademinia, M. Behzad, A. Alemi, M. Dolatyari, S. Maryam Sajjadi, RSC Adv. **5**, 71109 (2015)
41. S. Khademinia, M. Behzad, J. Nanoanalysis. **5**, 66 (2018)
42. R. Esmaeili, L. Kafi-Ahmadi, S. Khademinia, J. Mol. Struct. **1216**, 128124 (2020)
43. M. Khashaei, L. Kafi-Ahmadi, S. Khademinia, A.P. Marjani, E. Nozad, Sci. Rep. **12**, 8585 (2022)
44. A.E. Oksuz, M. Yurddaskal, U. Kartal, T. Dikici, M. Erol, J. Korean Ceram. Soc. **59**, 859 (2022)
45. S. Rajpoot, E.S. Kang, Y.-W. Kim, J. Korean Ceram Soc. **59**, 94 (2022)